We are IntechOpen, the world's leading publisher of Open Access books Built by scientists, for scientists

4,800
Open access books available

122,000
International authors and editors

135M
Downloads

Our authors are among the

154
Countries delivered to

TOP 1%
most cited scientists

12.2%
Contributors from top 500 universities

WEB OF SCIENCE™

Selection of our books indexed in the Book Citation Index in Web of Science™ Core Collection (BKCI)

Interested in publishing with us?
Contact book.department@intechopen.com

Numbers displayed above are based on latest data collected.
For more information visit www.intechopen.com

2

Heat Transfer for NDE: Landmine Detection

Fernando Pardo, Paula López and Diego Cabello
Universidad de Santiago de Compostela
Spain

1. Introduction

Although land mine problems existed in many regions, Bosnia (1995) and Afghanistan (2001) gave the land mine issue a particular sense of urgency. Intended for warfare, these mines remain buried after the end of the conflict. These mines are triggered by civilians causing around 15,000-20,000 victims per year in 90 countries, ICBL (2006). The U.S. State Department estimates that there are around 40-50 million of buried mines that need to be cleared. According to Horowitz (1996) 100,000 mines are found and destroyed per year; thus 450 years will be necessary to clean all mines. However, each year, 1.9 million of new mines are buried. In addition, the presence of mines also causes economic decline being one of the major limitations to agricultural work on these regions, Cameron & Lawson (1998). Thus, it is necessary to develop new techniques which allow to detect mines quickly and with high precision. The *Ottawa treaty*, Ottawa (1997), banning the production and use of AP mines was signed by 158 countries in 2007 however the most important AP manufacturers, China, Russia, India and EE.UU, have not yet signed it.
Nowadays more than 350 types of mines exist, Vines & Thompson (1999); but they can be broadly divided into two main categories:

- Antipersonnel (AP) mines.
- Antitank (AT) mines.

AT mines are relative big and heavy (2-5 Kg) and are usually laid on the ground forming regular patterns and shallowly buried. AT mines have enough explosive to destroy a tank or a truck, as well as to kill people in or around the vehicle; they also require more pressure to be detonated than AP mines. On the contrary AP mines contain less explosive and are lighter than AT mines. AP mines can be buried anywhere, they may lie on the surface or be shallowly buried. Sometimes they are placed in a regular pattern to protect AT mines, however in most cases they are placed randomly. Moreover, as AP mines are light and small, wind or rain can easily move them making their location, even with the original pattern, more difficult. AP mines are designed to damage foot soldiers avoiding their penetration into an specific area. These mines can kill or disable their victims and are activated by pressure, tripwire or remote detonation. These characteristics make AT mine detection and clearance easier than AP mine detection.
Detection and clearance of buried mines is a big problem with lots of humanitarian, environmental and economic implications. Current techniques for non-destructive evaluation

of soils fail to address the detection of small plastic landmines, which are the most difficult to detect. There is no universal technique capable of detecting buried landmines in all situations. The most widespread techniques in mine detection are metal detector and magnetometers. Magnetometers are used to detect ferromagnetic objects and they measure the disturbance of the earth's natural electromagnetic field. Many modern mines have almost no metal parts except for the small striker pin. Although metal detectors can be tuned to be sensitive enough to detect these small items (current detectors can track a tenth of a gram of metal at a depth of 10 cm), such sensitivity detects more metal debris and increases considerably the rate of false alarms. Increasing the sensitivity of metal detectors, therefore, does not solve the problem of non-metal mines satisfactorily. Taking in mind this limitation new techniques are appearing to detect the plastic landmines. Several techniques have been proposed for mine detection, such as acoustic techniques, Sabatier & Xiang (2001); X-rays techniques, Lockwood et al. (1997); biosensors, Larsson & Abrahamsson (1993); ion mobility spectrometers, Jankowski et al. (1992); nuclear quadrupole resonance, Englelbeen (1998); neutron analysis, Bach et al. (1996); ground penetrating radar (GPR) and infrared thermography (IRT), López et al. (2009); Thanh et al. (2009; 2007; 2008). Each technique has its advantages and disadvantages, for a more detailed description of theses techniques see Furuta & Ishikawa (2009); Gros & Bruschini (1998); López (2003); Robledoa et al. (2009); Siegel (2002).

Infrared thermography is an attractive technique for some mine detection tasks because it can be used from a considerable standoff distance, it provides information on several mine properties, and it can rapidly survey large areas. Its ability to detect mines has been recognized since the 1950s, Maksymonko & Le (1999). IRT sensors respond to electromagnetic radiation in a sensor-specific wavelength range. The source of the received signal may be either natural (i.e., thermal emission from the target or scattering of sunlight) or artificial (e.g., an infrared illuminator), which leads to both passive and active sensor concepts. Each material shows a characteristic thermal response to a given stimulus, also known as the *thermal signature*. Thus, the cooling or heating process affects buried objects and the surrounding soil in a different way. This difference is due to the fact that the mines are a better insulators than the soil. Thus, in the case of passive thermography, the soil layer over the mine tends to accumulate thermal energy during the day because the mine blocks the transport of thermal energy. As a result of this process the soil over the mine tends to be warmer than the surrounding soil. In the evening, the soil over the mine gives up thermal energy faster than the surrounding soil and results cooler. Around midday the soil and the mine reach the thermal equilibrium, which makes it impossible to perform the detection in this temporal gap. The main limitation of this technique is the fact that temperature differences strongly depend on the atmospheric conditions. On the other hand, active thermography uses artificial energy to heat the soil under study, avoiding the dependence on the atmospheric conditions. In spite of their long history, there is little compelling performance data available for infrared detection of antipersonnel mines.

The use of IRT as non-destructive evaluation (NDE) for landmine detection consists of subjecting the area under inspection to a source of natural or artificial heating/cooling process and studying the soil's response by means of the analysis of its thermal evolution given by a temporal sequence of infrared images. In this sense the study of the basic phenomenology lead to the development of mathematical models of the soil, England et al. (1992); England (1990); Kahle (1977); Liou & England (1998); Pregowski et al. (2000). The idea underneath is to

characterize, and therefore predict, the thermal behavior of the unperturbed soil under given conditions, i.e., its *thermal signature*. The presence of buried mines or other objects will alter this signature, which if manifested as a thermal contrast on the surface. From the analysis of this thermal contrast and, in particular of its dynamic evolution, it is possible to extract relevant information about the nature of the objects. A deep analysis of the evolution of the thermal contrast over a diurnal cycle can be found in Khanafer & Vafai (2002), where the conditions for detection are studied, and sunrise and sunset are established as the periods of the day in which the presence of buried mines induces a greater thermal contrast on the surface (around 4-6°C).

An efficient way of extracting information from this data regarding the presence of landmines using a 3D thermal model of the soil based on the solution of the heat equation was presented in López et al. (2009; 2004). The process is divided in two steps. On the first one, the forward problem, the soil is subjected to a heating process and a comparison between temperatures measured at the soil surface (through IR imaging) and those obtained by simulation using the model under the assumption of homogeneous soil and mine absence is made. The differences between measured and simulated data put into evidence the presence of unexpected objects on the soil. The second step is an inverse engineering problem where the thermal model must be run for multiple soil configurations representing different types of possible targets (mine, stone, ...) and depths of burial. The nearest configuration to the measured data give us the estimated nature and location of the targets. This approach and, particularly, the inverse engineering process, makes an intensive use of the 3D thermal model that needs to be solved iteratively involving complex, coupled sets of partial differential equations. The extensive computing power required makes impractical its software implementation in personal computers . An alternative solution is the hardware implementation of the Finite Difference (FD) representation of the thermal model. In fact, different hardware implementations of FD solutions in the electromagnetics domain can be found in the literature, Durbano et al. (2004); Placidi et al. (2002); Schneider et al. (2002). In previous works, Pardo et al. (2009; 2010), we have presented an FPGA implementation of a FD Heat Equation solver which speeds the computation up by a factor of 10 compared to the purely software solution. The bottleneck of such an implementation is the access to memory and the amount of available memory, which dramatically reduces the performance of the system. However, this solution is hardware dependent an its cost is quite high. In recent years, Graphic Processing Units (GPUs) have been proved to be a valuable hardware platform to solve problems with a high degree of parallelism, Hwu et al. (2008). The total speedup of the system in a typical simulation setup by a factor 40 compared to a Core2Duo 2.8 GHz implementation in C++, using a NVIDIA GTS250 GPU, but even higher speedups could be achieved with more advanced GPUs.

The chapter is outlined as follows. In Section 2 the thermal model and the detection algorithm are introduced. Section 3 addresses the architecture of the hardware implementation and its GPU projection details. In Section 4 the main results are shown and, finally, the conclusions are summarized.

2. Infrared thermography for NDE

Infrared thermography sensors, which respond to electromagnetic radiation in a sensor-specific wavelength range, constitute an attractive NDE technique because they can

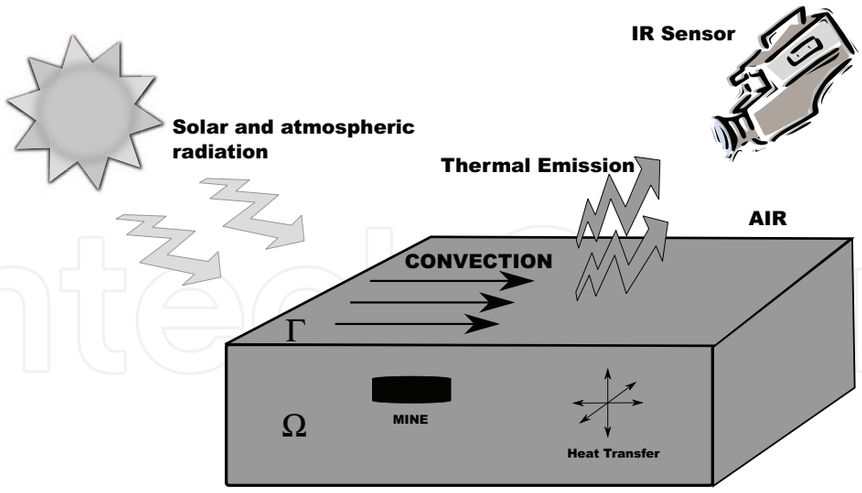

Fig. 1. Different heat transfer processes taking place in the soil volume and at the air-soil interface.

be used from a considerable standoff distance to rapidly survey large areas while providing information on several properties. Different materials show a characteristic response to a given thermal stimulus over time, a property that can be successfully used for the identification of buried targets. We will present a general procedure for the inspection of soils based on the solution of the heat equation applied, but not limited, to the detection of plastic antipersonnel mines.

2.1 Thermal model of the soil

The main processes considered are summarized in Fig. 1. We consider a soil volume, Ω, subjected to a known thermal stimulus through the soil-air interface, Γ, where both the soil and the targets are modeled as isotropic objects. We also assume that the thermal diffusivity is constant and that the temporal variation of the moisture content and the mass transference during the time of analysis are negligible, which are fair assumptions as long as the duration of the experiment does not exceed a couple of hours and the depth of inspection is limited to 10-15cm. A typical example is antipersonnel mine detection, given that mines are usually either laid on the surface or only shallowly buried. Moreover, empirical evidence demonstrates that it is possible to reduce the interval of interest to roughly one hour around sunrise or sunset as it is at these times when their different thermal evolution is more clearly manifested. Under these assumptions the overall process is described by the time-dependent single-phase 3D heat equation:

$$\frac{\partial T(\overrightarrow{r},t)}{\partial t} - div\left(\alpha(\overrightarrow{r})\ grad\ T(\overrightarrow{r},t)\right) = 0 \ \ ,\alpha = \frac{k}{\rho c_p} \tag{1}$$

where $\overrightarrow{r} = (x,y,z)$ with $r \in \Omega$, ρ [kg/m^3] is the density, c_p[J/kg K] is the specific heat, k[W/m K] is the thermal conductivity, α [m^2/s] is the thermal diffusivity and T [K] is the distribution of temperatures inside the soil. To solve this equation the initial and boundary

conditions are required:

$$k\frac{\partial T(\overrightarrow{r},t)}{\partial n} = q_{net}(t) \quad for\ \tau\ \times\ \Gamma \tag{2}$$

$$\frac{\partial T(\overrightarrow{r},t)}{\partial n} = 0 \quad for\ \tau\ \times\ \partial\Omega\backslash\Gamma \tag{3}$$

$$T(x,y,z\rightarrow\infty,t) = T_{\infty} \tag{4}$$

$$T(\overrightarrow{r},t=t_0) = T_0(\overrightarrow{r}) \quad in\ \ \Omega \tag{5}$$

where τ is the time interval of analysis, q_{net} is the net heat that flows through the soil-air interface Γ, n is the normal to the surface under consideration $\partial\Omega$. Eq. (2) gives the boundary condition at the air-soil interface; Eq. (3) shows the boundary conditions applied to the sides of the volume not accessible for measurements, imposing a vanishing heat flux across them. Eq. (4) is the deep-ground condition and it establishes that the temperature at a large enough depth remains constant. Finally, Eq. (5) gives the initial conditions for the system. The net heat flux at the soil-air interface, q_{net}, in Eq. (2) can be written as:

$$q_{net}(t) = q_{sun}(t) + q_{rad}(t) + q_{conv}(t) \tag{6}$$

where q_{sun} is the short-wave radiation emitted by the sun and absorbed by the soil; q_{conv} represents the convection term at the soil-air interface; and q_{rad} is the heat flux exchange due to radiation. The first term of this expression, q_{sun}, can be easily measured with the help of low-cost equipment. The second term is given by $q_{\mathrm{rad}}(t) = q_{\mathrm{sky}}(t) - q_{\mathrm{soil}}(t)$. The term $q_{\mathrm{sky}}(t)$ is the longwave radiation from the atmosphere given by Stefan's law. Finally, the third term in Eq. (6) can be approximated by, $q_{\mathrm{conv}}(t) = h(T_{\mathrm{air}}(t) - T_{\mathrm{soil}}(t))$, where h [W/m^{2}K] is the convective heat transfer coefficient that is known to depend strongly on the wind speed.

2.2 Algebraic equations

Eq. (1) can be solved applying a FD approach, using either implicit or explicit methods. Using the explicit method a set of equations that can be solved sequentially is obtained, its main advantages being the simplicity of the formulation and its direct hardware translation. This method, however, is only conditionally stable, Bejan (1993). On the other hand, the implicit schemes are unconditionally stable but require the solution of the whole set of equations simultaneously. The ADI method, Wang & Chen (2002), can overcome the drawbacks of these two methods using a mixed approach, where only a subset of equations must be solved simultaneously while retaining the unconditional stability property. Thus, high temporal discretization steps can be used, effectively reducing the computing time when, for instance, a system evolving toward a steady state is studied. However, in our case, the boundary conditions change during the simulation time making necessary the use of small temporal discretization steps and, therefore, the benefit of using an ADI method is lost. Due to this fact and to the simplicity of the equations obtained, which allows to easily perform a hardware implementation, we have chosen an explicit scheme to solve the heat equation. Under this approach the derivatives can be approximated as:

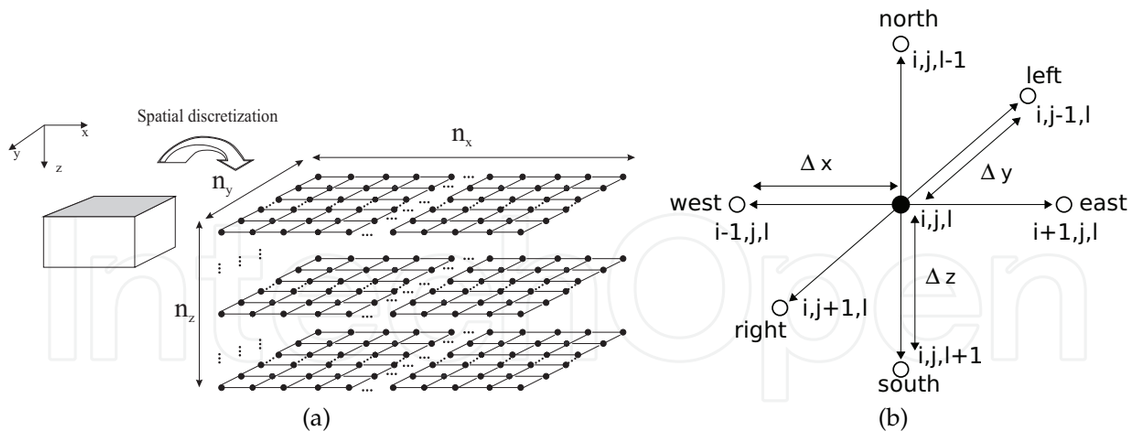

Fig. 2. (a) Spatial discretization scheme of the continuous soil into a set of discrete nodes. (b) Considered neighbors to perform the updating process.

$$\frac{\partial^2 T(\mathbf{r},t)}{\partial x^2} \approx \frac{T_{i+1,j,l} - 2T_{i,j,l} + T_{i-1,j,l}}{(\Delta x)^2} \tag{7}$$

$$\frac{\partial T(\mathbf{r},t)}{\partial t} \approx \frac{T^{m+1} - T^m}{\Delta t} \tag{8}$$

where Δx and Δt are, respectively, the spatial and temporal discretization steps; i, j, l are the discretization indexes in the x, y and z directions respectively and m is the time discretization index. The spatial discretization scheme of the continuous soil into a mesh of discrete nodes can be seen in Fig. 2(a), where n_x, n_y and n_z represent the number of nodes in the x, y and z directions respectively ($i = 0, 1, ...n_x - 1$, $j = 0, 1, ...n_y - 1$ and $l = 0, 1, ...n_z - 1$). Applying this discretization scheme to Eq. (1), we obtain the following equations for a surface ($T_{i,j,0}$) and an internal node ($T_{i,j,l}$, with $l > 0$), assuming, without loss of generality, that the spatial discretization steps are the same in all directions, that is, $\Delta x = \Delta y = \Delta z$,

$$\begin{aligned} T^{m+1}_{i,j,0} = T^m_{i,j,0} + F_0[&\sum_{neighbors\ surface} (T^m_{neighbor} - T^m_{i,j,0}) + 2(T^m_{i,j,1} - T^m_{i,j,0})] \\ &+ 2\alpha_{sun} F_0 S q^m_{sun} + (2F_0 H + 8F_0 R T^3_{air})(T_{air} - T^m_{i,j,0}), \quad \forall i,j \end{aligned} \tag{9}$$

$$T^{m+1}_{i,j,l} = T^m_{i,j,l} + F_0 \sum_{neighbors} (T^m_{neighbor} - T^m_{i,j,l}), \quad \forall i,j,l > 0 \tag{10}$$

where $F_0 = F_0(i,j,l)$, R, S and H are defined as,

$$F_0 = \frac{\alpha \Delta t}{(\Delta x)^2} \qquad R = \frac{\sigma \epsilon}{k} \Delta x \qquad S = \frac{\Delta x}{k} \qquad H = hS. \tag{11}$$

As seen, every new temperature, T^{m+1}, is calculated as a function of the temperatures in the previous time step, T^m, and only the nearest neighbors are considered in order to facilitate the hardware implementation, see Fig. 2(b). In the case of the surface layer, only the neighbors in

the same layer ($z = 0$) and in the layer beneath ($z = 1$) are considered. Using the explicit FD method Eq. (10) can be written as,

$$T_{i,j,l}^{m+1} = T_{i,j,l}^{m}(1 - 6F_0) + F_0(T_{i+1,j,l}^{m} + T_{i-1,j,l}^{m} + T_{i,j+1,l}^{m} + T_{i,j-1,l}^{m} + T_{i,j,l+1}^{m} + T_{i,j,l-1}^{m}) \quad (12)$$

Thus, for an internal node the instability is avoided if the term $(1 - 6F_0)$ of Eq. (12) is non negative, (Bejan, 1993; Incropera & DeWitt, 2004), which is translated into a small enough Δt such that,

$$F_0 = \frac{\alpha \Delta t}{(\Delta x)^2} \leq \frac{1}{6} \quad (13)$$

As can be noted, the stability criteria is a trade-off between the spatial and temporal discretization steps. The small size of the mines constraints the value of Δx, which must be small enough to have several nodes representing the mines. Thus, a small value of Δx must be chosen which also implies to choose a small value of Δt. Meanwhile for a surface node Eq. (9) the stability criteria can be written as:

$$\begin{aligned} T_{i,j,0}^{m+1} = T_{i,j,0}^{m}(1 - 6F_0 - 2F_0H - 8F_0RT_{air}^3) + \\ F_0(T_{i+1,j,0}^{m} + T_{i-1,j,0}^{m} + T_{i,j+1,0}^{m} + T_{i,j-1,0}^{m} + 2\,T_{i,j,1}^{m}) + \\ (2F_0H + 8F_0RT_{air}^3)T_{air} + 2\alpha_{sun}F_0Sq_{sun}^{m} \end{aligned} \quad (14)$$

Resulting in the following stability condition for a surface node:

$$F_0 \leq \frac{1}{6 + 2H + 8RT_{air}^3}. \quad (15)$$

As shown, the maximum Δt for a given Δx is limited by the condition on F_0.
In summary, applying the FD method, the thermal model of the soil is discretized into a set of nodes whose thermal behavior is given by algebraic equations involving additions, subtractions and multiplications, making it suitable for a hardware implementation.

2.3 IRT-based soil inspection for the detection of buried objects

Many physical systems are characterized by the solution of a differential equation or system of equations subject to known boundary conditions. This is the called *forward problem*. The representation of a non-linear forward operator can take the form of a functional equation involving a map F, which represents the connection between the model and the data:

$$y = F[p] \quad (16)$$

where F is a non-linear operator between Hilberts space Y and P, y is the measured data and p the original distribution of parameters that gives rise to y under the application of operator F. An *inverse problem* of this will be the reconstruction of the original distribution of parameters based on the measurements of the resulting data.
Solving an inverse problem implies approximating the best solution $p^{\dagger} = F^{-1}[y]$ of Eq. (16). In general, $y \in Y$ is never known exactly but up to an error of $\delta \neq 0$. Therefore, we assume

that we know $\delta > 0$ and $y^\delta \in Y$ with $\|y - y^\delta\| \leq \delta$. Thus, y^δ is the *noisy* data and δ is the noise level. Under these situations is, generally, impossible to compute numerically a solution of the problem unless making use of the regularization techniques, which makes it possible to restore stability and existence/uniqueness of the solution and develop efficient numerical algorithms, Kirsch (1996).
An example of such a technique is the non-linear Landweber iteration method which is defined by the following recursive procedure, Engl et al. (1996):

$$p_k^\delta = p_{k-1}^\delta + F'[p_{k-1}^\delta]^T(y^\delta - F[p_{k-1}^\delta]) \quad k \in \mathbb{N} \tag{17}$$

As initial guess $p_{k=0} = p_0$ is set, incorporating a *priori* knowledge of an exact solution $p^\dagger$. For non-linear problems, additional conditions about the stopping rule have to be imposed to guarantee convergence rates, Engl et al. (1996). The inequality known as the *discrepancy principle* will be used to define the stopping index $k(\delta, y^\delta)$ with

$$\|y^\delta - F[p_{k(\delta,y^\delta)}]\| \leq \mu\delta < \|y^\delta - F[p_k^\delta]\| \quad 0 \leq k \leq k(\delta, y^\delta) \tag{18}$$

if the parameter μ is chosen subject to the constraint

$$\mu > 2\frac{1+\eta}{1-2\eta} \tag{19}$$

being $\eta < 1/2$. The proof that this stopping rule regularizes the Landweber iteration method can be found in Engl et al. (1996).
Once the convergence criteria and the stopping rule have been established, the iterative procedure is applied to update the estimate of the solution in practical situations. It can be seen that the update term in the Landweber iterative method, see Eq. (17), is the negative gradient at $p = p_{k-1}^\delta$ of the functional

$$J = \|F[p] - y^\delta\| \tag{20}$$

that is the misfit between the model and the measured data. Solving the inverse problem is hence equivalent to minimize this functional.
The solution of the forward problem, F, is then the solution of the system of Eqs. (1)-(4) given the boundary conditions in the surface of the soil, Γ, and a distribution of soil parameters p within the volume Ω. According to Eq. (1), p corresponds to the value of the thermal diffusivity at every point within the soil volume, $\alpha = \alpha(x, y, z)$. Given the 3D nature of the model, the application of the operator F to the set of parameters, p, produces a 3D solution where the distribution of temperatures both on the surface and within the soil volume is calculated. For the sake of clarity we denote as $F[p]$ the distribution of the temperatures on the surface of the soil, which is compared with the temperature distribution acquired by the IR camera, our noisy data y^d. The reconstruction of the internal composition of the soil can be viewed as an inverse problem of this,that can be formulated as: *given the boundary conditions of the system and a distribution of measurements y on* Γ*, derive the soil parameter distribution,* p*, within* Ω*, that is,* $p = F^{-1}[y]$.
Now we will introduce the procedure for the non-destructive inspection of soils for the identification and classification of mines and mine-like targets on infrared images based on the

solution of the heat equation and the use of inverse problems techniques, López (2003); López et al. (2009; 2004). The process starts with the acquisition of a sequence of infrared images of the surface of the soil under known heating and atmospheric conditions. As explained before, sunrise and sunset are the preferred times for detection. We will also assume that a pre-processing stage is run on a conventional PC in order to align the images and map grayscale colors to temperature values on the surface. Next, the soil inspection procedure itself starts. First, we run a detection procedure, as will be explained in the following section, to obtain the mask of potential targets. Then, a quasi-inverse process operator is used to identify the presence of antipersonnel mines among the potential targets. For those targets that failed to be classified as mines (and are therefore labeled as *unknown*), a full inverse procedure to extract their thermal diffusivity will be run in order to gain information about their nature. The overall detection process is summarized in Fig. 3, where the processes that require the use of the 3D thermal model are indicated with an ellipse. The detection, quasi-inverse and full-inverse procedures are based on the solution of the heat equation for different soil configurations. As explained, this is a very time consuming task that makes the whole algorithm inefficient for real on-field applications.

2.3.1 Target detection

The use of IR cameras taking images of the soil under inspection gives us the exact distribution of temperatures on the surface. On the other hand, the thermal model described previously and extensively validated with experimental data permits us to predict the thermal signature of the soil under given conditions, López (2003); López et al. (2004). The detection of the presence of potential targets on the soil is then made by comparing the measured IR images with the expected thermal behavior of the soil given by the solution of the forward problem under the assumption of absence of mines on the field, mathematically,

$$\alpha(x,y,z) = \alpha_{soil}, \qquad \forall x,y,z. \tag{21}$$

For this set of soil parameters, p, the application of the functional in Eq. (20) determines the surface positions (x,y) where the behavior is different from that expected under the assumption of mine absence, therefore revealing the presence of unexpected objects on the soil. These positions will be classified as potential targets, whereas the rest of the pixels (those that follow the expected pure-soil behavior) will be automatically classified as *soil*. This process is not trivial. The most straightforward approach, the thresholded detection, has the drawback of setting the threshold, which will vary not only for different image sequences, but it is also likely to depend on the particular frame of the sequence, and on the characteristics of the measured data such as lighting conditions and the nature and duration of the heating. For this reason, the use of a reconfigurable structure, capable of adapting to varying experimental conditions was proposed on López (2003); López et al. (2004). In this work they demonstrated that it is possible to reduce the time frame of analysis to roughly one hour around sunrise as it is at this time when the maximum thermal contrast at the surface is expected. This phenomena can be better appreciated in Fig. 4, where a sequence of IR images of a mine field taken between 07:40 am and 08:40 am is shown. Taking into account the short time interval we can consider that the properties of the soil remain unaltered and that there is no mass transference process during the simulation. The output of the detection stage is a black and white image with the mask of the potential targets.

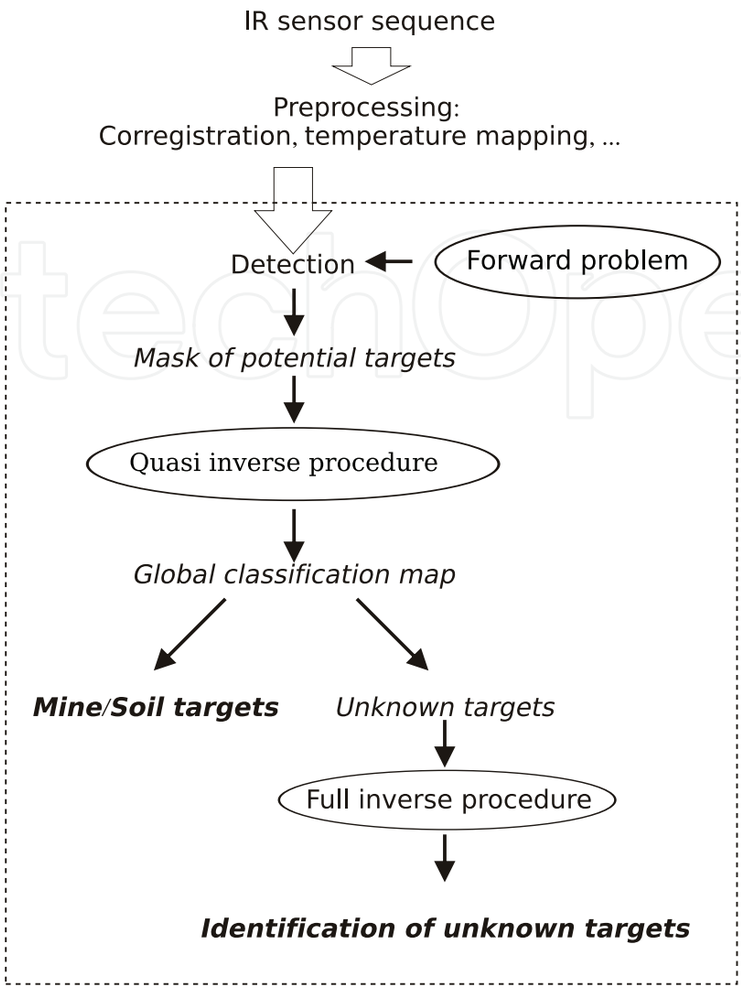

Fig. 3. Structure of the approach used to detect buried landmines using infrared thermography.

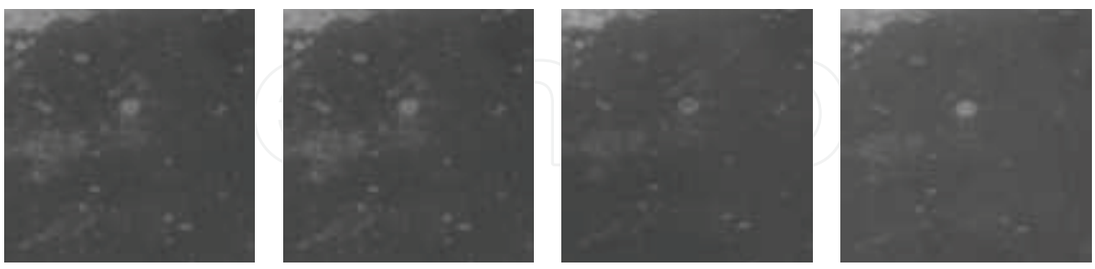

(a) 7:40 am (b) 08:00 am (c) 08:30 am (d) 09:00 am

Fig. 4. Measured IR images of a minefield at sunrise.

2.3.2 Quasi-inverse operator for the classification of the detected targets

In the previous section we dealt with the identification of the (x, y) position of the potential targets on the soil. In this section we will propose an operator for their classification into either *mine* or *soil* categories; any target that fails to fit into these categories will be

classified as *unknown* (a procedure for the retrieval of further information about the nature of the *unknown* targets will be explained in the next section). For the *mine* category, the depth of burial will be also estimated. In general, this reconstruction is not possible unless additional information on the solution is incorporated in the model by means of the so-called *regularization techniques* Engl et al. (1996); Kirsch (1996). It is, however, possible to solve the inverse problem without the explicit use of a regularization strategy under proper initialization conditions and the use of iteration methods.
The iterative procedure is based on evaluating Eq. (20), which expresses the deviation between the observed IR data, y^{δ}, and the one given by the solution of the forward problem using known parameter distributions, $F[p]$. Therefore the heat equation needs to be solved for each of these distributions during the time of analysis (usually one hour around sunrise). In the case of mine targets, we will assume that their thermal evolution is driven by the thermal properties of the explosive used, which is commonly TNT composition B-3 or, less frequently, Tetryl. Our initial guess will be to assume that, *(i)* all the targets detected in the detection step are mines, that is,

$$\alpha_{\text{target}} = \alpha_{\text{mine}}, \tag{22}$$

and *(ii)* the possible depths of burial constitute a discrete set $z \in \tilde{Z}$ being,

$$\tilde{Z} = \{k\,\Delta z, \quad \forall k = 0, 1, ..., d\}, \tag{23}$$

with Δz the discretization step and $d\,\Delta z$ the a depth of burial at which is satisfied the deep-ground condition, see Eq. (4). The situation $k = 0$ corresponds to surface-laid mines. These two assumptions imply a reduction of the search space, therefore the *quasi*-inverse nature of the classification effort that will either confirm or reject them. Let,

- $\{y_s^{\delta}\}$, $s = 1, ..., S$, be the acquired IR image sequence, being S the total number of frames.
- $F[p]_{s,k}$, the modeled temperature distribution on the soil surface at time s. $F[p]_{s,k}$ is estimated by considering that all the detected targets are landmines buried at the depth given by index k in Eq. (23).

Note that, in the following, we will concentrate only on those areas of the image that were marked as possible targets in the detection phase. The classification map for the detected targets is obtained through the definition of a classification operator which includes the following computations:

1. For each time instant $s = 1, ..., S$ and burial depth $k = 0, ..., d$, an error map, $J_{s,k} = \|F[p]_{s,k} - y_s^{\delta}\|$, is estimated by evaluating Eq. (20) for each pixel position (x, y);
2. For each time instant s, a global error map (J_s) and a global classification map (Y_s) are estimated iteratively by comparing the error maps $J_{s,k}$, $k = 0, ..., d$, as follows:
   - *Initialization step:* For each pixel (x, y), we set $J_s(x, y) = \varepsilon$ (where ε is a predefined threshold error value); and $\mathrm{Y}_s(x, y) = soil$.
   - *Iterative update step:* For each depth of burial, k, with $k = 0, ..., d$, $J_s(x, y) = min(J_{s,k}(x, y), J_s(x, y))$ and $\mathrm{Y}_s(x, y) = argmin_k(J_{s,k}(x, y), J_s(x, y))$ (the category for which the error is smaller, i.e. the depth of burial). If $J_s(x, y) > \varepsilon$ then $\mathrm{Y}_s(x, y)$ is set to $Unknown$.
3. Once J_s and Y_s have been obtained, we combine all these partial maps (J_s, resp. Y_s) into single ones ($\mathbf{J}$, resp. $\mathbf{Y}$) in the following way:

- **Y**: Pixels classified as mines at any processing step are kept in the final classification map. For the others, we keep the category that appears more times.
- $\mathbf{J}(x,y) = max_s(J_s(x,y))$. This is a very conservative approach aiming at reducing the number of false negatives (failure to detect a buried mine) even at the cost of increasing the false alarm rate of the system.
- To find a trade-off between the accuracy of the classification and the number of false alarms, we define a *cutoff error*, e_{max}. If the entry on the error map, **J** for a pixel exceeds e_{max}, the pixel will be automatically assigned to the category of *Unknown*. e_{max} is estimated empirically, however it could be estimated taking into account the pixels classified as non-mine based their temperature variance using bootstrap techniques, Zoubir & Iskander (2004).

2.3.3 Full-inverse procedure for the classification of non-mine targets

In this case, no assumption about the nature of the targets found in the detection phase is made, although the set of possible depths at which the targets can be placed is still bounded by Eq. (23). Under these assumptions, Eq. (22) does not hold and α_{target} is unknown and could take any value depending on the nature of the object. For this reason, it is necessary in this case to use a systematic approach for the minimization of the functional J, which implies the calculation of the gradient $\partial J/\partial p$.

Let us consider the existence of a buried target in a 3D soil volume, Ω, with an unknown $\alpha = \alpha(r)$, $r = (x,y,z) \in \Omega$. The thermal experiment is the following: at time $t = t_0$, the solid is subject to a prescribed flux, $q_{\text{net}}(r',t)$, on its surface Γ, being Γ the portion of the surface $\partial\Omega$ accessible for measurements. We then measure the temperature response $\theta(r',t)$ at the boundary $r' \in \Gamma$, during the time interval $[t_0, t_f]$. We rewrite our 3D forward problem in Eq. (1) as,

$$-\text{div}\{\alpha(r)\,\text{grad}\theta\} + \tfrac{\partial\theta}{\partial t} = 0, \quad r \in \Omega \tag{24a}$$

$$\theta(r, t = t_0) = \theta_0, \quad r \in \Omega \tag{24b}$$

$$\tfrac{\partial}{\partial n}\theta(r',t) = q_{\text{net}}(r',t) \quad r' \in \Gamma,\, t \in [t_0, t_f]. \tag{24c}$$

We look at the reconstruction of $\alpha(r)$ from the knowledge of the surface response of temperature, $y^\delta = \theta(r',t)$, to prescribed flux applied on the boundary $q_{\text{net}}(r',t)$. We call *data* the pair $(\theta(r',t), q_{\text{net}}(r',t))$. As mentioned before, this is an ill-posed problem. It is intuitive that the data parameters (r',t) belong to a 3D subset, because $r' \in \Gamma$ and $t \in [t_0, t_f]$. This is sufficient enough for the reconstruction of the function $\alpha(r)$, defined in a 3D volume. Let us now introduce the *model* problem as an initial guess p, such that $p(r') = \alpha(r')$ (known data on the boundary), with the following governing equations and boundary conditions,

$$-\text{div}\{p(r)\,\text{grad}u\} + \tfrac{\partial u}{\partial t} = 0 \quad r \in \Omega \tag{25a}$$

$$u(r, t = t_0) = u_0, \quad r \in \Omega \tag{25b}$$

$$\tfrac{\partial}{\partial n}u(r,t) = q_{\text{net}}(r',t) \quad r' \in \Gamma, t \in [t_0, t_f]. \tag{25c}$$

The solution of Eq. (25) is a well-posed problem, as opposed to Eq. (24), and will be denoted by $u(r,t;p)$. Our aim will be to control p in such a way that the difference between the model and the observed data tends to zero. This goal is quantified by an objective function J to be

minimized. The functional to be minimized is the L^2 norm of the misfit between the model and the observation given by,

$$J(u(p)) \equiv \frac{1}{2} \int_{t_0}^{t_f} \int_{\Gamma} \|u(r',t;p) - \theta(r',t)\|^2 dS\, dt. \tag{26}$$

This is a classic optimization problem which implies the calculation of the gradient of the functional J. To this aim we will make use of the variational method. If we introduce the notation,

$$\begin{aligned} < u, v >_{\Omega} &= \int_{\Omega} u(r)\, v(r)\, d\Omega \\ < q_{\text{net}}, v >_{\Gamma} &= \int_{\Gamma} q_{\text{net}}(r')\, v(r')\, dS \\ a_p < u, v > &= \int_{\Omega} p\, \text{grad}u\, \text{grad}v\, d\Omega, \end{aligned}$$

then the model problem, Eq. (25), is equivalent to the variational problem,

$$\int_{t_0}^{t_f} < \frac{\partial u}{\partial t}, v >_{\Omega}\ dt + \int_{t_0}^{t_f} (a_p < u, v >)\, dt - \int_{t_0}^{t_f} < q_{\text{net}}, v >_{\Gamma}\ dt = 0,\ \forall v \tag{27}$$

Eq. (27) can be considered as the constraints in the minimization problem, see Eq. (26). Therefore, we can introduce the Lagrange multiplier $\lambda(r,t)$ and define the Lagrangian L as,

$$L(u,p,\lambda) \equiv J(u) + \int_{t_0}^{t_f} \{< \frac{\partial u}{\partial t}, \lambda >_{\Omega} + a_p < u, \lambda > - < q_{\text{net}}, \lambda >_{\Gamma}\}\, dt. \tag{28}$$

Note that $L = J$ if u is the solution of the model problem, Eq. (25), since Eq.(27) holds for any λ. Thus, the minimum of J under the constraints in Eq. (27) is the stationary point of the Lagrangian L. Conversely, if $\delta L = 0$ for arbitrary $\delta\lambda$, u and p being held fixed, it follows necessarily that Eq. (27) holds. We consider,

$$\delta L = \frac{\partial L}{\partial u}\delta u + \frac{\partial L}{\partial p}\delta p, \tag{29}$$

where,

$$\frac{\partial L}{\partial u}\delta u \equiv \int_{t_0}^{t_f} (u - \theta, \partial u)_{\Gamma}\, dt + \int_{t_0}^{t_f} \{(\delta \frac{\partial u}{\partial t}, \lambda)_{\Omega} + a_p(\delta u, \lambda)\}\, dt \tag{30a}$$

$$\frac{\partial L}{\partial p}\delta p \equiv \int_{t_0}^{t_f} \int_{\Omega} \delta p\, \text{grad}u\, \text{grad}\lambda\, d\Omega\, \delta\mu. \tag{30b}$$

We can restrict the choice of λ such that

$$\frac{\partial L}{\partial u}\delta u = 0. \tag{31}$$

This condition can be written as,

$$\int_{t_0}^{t_f} < u - \theta, \delta u >_{\Gamma}\ dt + \int_{t_0}^{t_f} \{- < \delta u, \frac{\partial \lambda}{\partial t} >_{\Omega} + a_p < \delta u, \lambda >\}\, dt + < \delta u, \lambda >_{\Omega} |_{t_0}^{t_f} = 0, \tag{32}$$

where $\delta u(x,0) = 0$. The last term of (32) vanishes if we impose,

$$\lambda(r, t \geq t_{\mathrm{f}}) = 0. \tag{33}$$

By doing so we obtain the equation for the adjoint field λ,

$$-\mathrm{div}\{p\,\mathrm{grad}\lambda\} - \tfrac{\partial \lambda}{\partial t} = 0, \quad r \in \Omega \tag{34a}$$

$$\lambda(r, t \geq t_{\mathrm{f}}) = 0, \quad r \in \Omega \tag{34b}$$

$$\tfrac{\partial}{\partial n}\lambda(r', t) = \theta - u, \quad r \in \Gamma. \tag{34c}$$

This is the so called *back diffusion* equation for the adjoint field, and it is also a well posed problem. With this choice of the adjoint field $\lambda(r,t)$, the variation ∂J becomes

$$\partial J = \int_{t_0}^{t_{\mathrm{f}}} \int_{\Omega} \partial p\,\mathrm{grad}u\,\mathrm{grad}\lambda\, d\Omega\, dt. \tag{35}$$

It results from Eq. (35) that the derivative of J in the $p(r)$ direction is known explicitly by solving two problems, the direct problem for the field u and the adjoint problem for the field λ. That is, the Z-integral,

$$\frac{\partial J}{\partial p} \equiv Z = \int_{t_0}^{t_{\mathrm{f}}} \mathrm{grad}u\,\mathrm{grad}\lambda\, dt. \tag{36}$$

Solving Eq. (25) and Eq. (34), both of them well-posed forward problems, and using Eq. (36), the expression of the update of Eq. (17)) can be calculated in a straightforward manner. With respect to the number of iterations of the Landweber method, the selection of the stopping criteria of the algorithm must be made according to the discrepancy principle in Eq. (18)). The bigger the η, the lower the number of iterations is, and the higher the error is. The selection of η for a particular application must then be a trade-off between computational time and accuracy of the solution.

2.4 Estimation of the computational cost

The algorithm described above is based on iterative procedures involving multiple solutions of the heat equation for different soil configurations. This constitutes a time consuming process not feasible for its use on the field as the computational complexity of the FD method, if $N = n_x \cdot n_y \cdot n_z$ is the total number of grid nodes, is O($N \cdot IT$), where IT is the number of iterations. As an example, we consider the analysis of a piece of soil ($\alpha_{soil} = 6.4 \cdot 10^{-7}$ m/s^2) of moderate dimensions of 1m×1m with a shallowly buried mine ($\alpha_{mine} = 2.64 \cdot 10^{-7}$ m/s^2). Even if the depth resolution of IRT is barely 10-15 cm, the depth of analysis must be set to at least 40-50 cm in order to apply the boundary condition in Eq. (4). Using a uniform spatial discretization of $\Delta x = \Delta y = \Delta z = 0.8$ cm and assuming a temporal discretization step of $\Delta t = 6.25$ s ($F_0 = 0.06$), for a typical example the simulation of the behavior of the soil during one hour using C++ (optimized for speed using O2 flag from Microsoft Visual C++ compiler) on a Intel Core2Duo 2.8GHz takes 30 seconds if single precision arithmetic is used to represent the temperatures. Taking into account that the proposed inverse procedure requires the solution of the model for multiple soil configurations, the total computing time assuming that only 100 iterations are needed (a soft approach) will add up to 50 minutes. As this jeopardizes its use for field experiments we have developed a hardware implementation of a

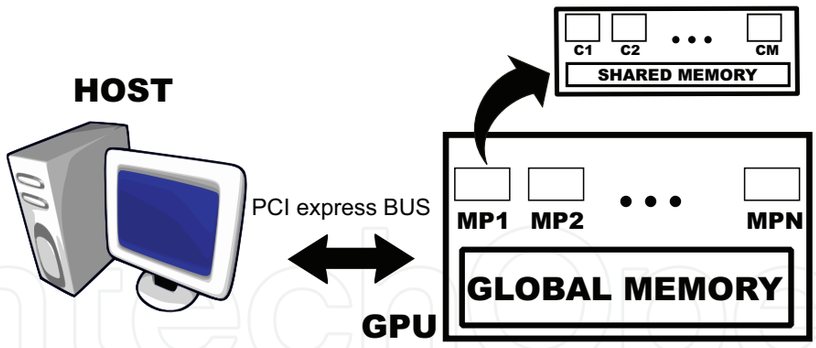

Fig. 5. GPU internal structure and memory hierarchy.

heat equation solver. In Pardo et al. (2009; 2010) we presented an FPGA-based implementation of such a solver. However, the main drawback of an FPGA implementation is the requirement of the system in terms of memory. The FPGA has a little amount of distributed memory and the FPGA's logic blocks can also be configured to behave like memory, however this is an inefficient way of FPGA using. Some vendors offer cards where external memory and FPGA are integrated on the same board, allowing to use the FPGA to deal with processing issues. However, these are expensive solutions. GPUs offers a structure which perfectly fits with the proposed problem and they have the advantage of being cheaper than FPGAs. GPUs are present in all computers and therefore we avoid the necessity of having a dedicated and expensive hardware to deal with our problem. Moreover, the GPU implementation is hardware independent, in the sense that it can be used on GPUs from NVIDIA with none or little changes, depending on GPU's computing capabilities.

3. GPU thermal model implementation

The system that solves the thermal model using the explicit FD method was implemented using CUDA language, NVIDIA (2010), and projected in a GPU from NVIDIA. The computing structure of GPUs makes them a suitable candidate to implement algorithms requiring high computing power. First we will introduce GPU characteristics and some basics abouts its programming mode. Then, we will present the proposed GPU implementation that simulates the thermal behavior of the soil and that speeds the computations up compared to a personnel computer.

3.1 GPU structure

GPUs are made up of several multiprocessors that can perform parallel processing data, which makes them suitable for processing in systems where it can be split up in independent portions and processed independently. The structure of such a GPU can be seen in Fig. 5. The GPU is made up of several multiprocessors, labeled as MP1 ... MPN in Fig. 5. Moreover, inside each multiprocessor there are several cores, labeled as C1 ... CM in Fig. 5. One important issue of GPU programming concerns to the use of the different memories available in the GPU, see Fig. 5. The *Global Memory* is available to all multiprocessors and cores, whereas the *Shared Memory* inside each multiprocessor is only available to the corresponding multiprocessor's cores. Additionally, each core has its own and private memory space. One key aspect of a GPU-based system is the memory data organization and access, as they can impose a

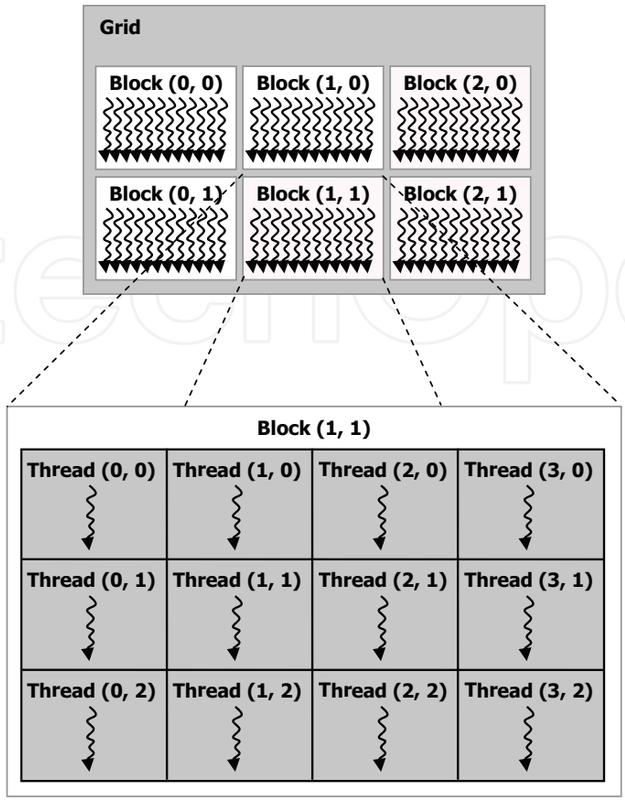

Fig. 6. Structure of threads hierarchy in a GPU (reprinted from NVIDIA (2010)).

bottleneck in the system performance. The global memory has an access latency two orders of magnitude higher than the access to the shared memory. Thus, it is important to minimize the use of global memory and maximize, as far as possible, the use of shared memory because this will increase the performance of the system.

Once the structure of the GPU has been briefly described we will introduce the basic aspects of GPU programming required to understand the structure of the proposed system . Functions in CUDA are called *kernels* and each kernel can be executed in parallel by several threads[1], as contrary to ordinary C/C++ functions that can only be executed by one processor. A kernel is not executed as a single thread, but it is executed as a block of threads, each of them processing the same function on different data, following a single-program multiple data (SPMD) computing model. Each thread inside the block has a 1D, 2D or 3D identifier (ID), depending on the applications, which distinguishes the concrete thread, to compute elements from a vector, matrix or volume of data. All the threads of a block are executed on the same multiprocessor and therefore they must fit within the available resources. This sets a limit on the maximum threads per block, which is limited to 512 in current GPUs. To avoid this limitation a kernel can be executed in several blocks of threads, which are organized as 1D or 2D groups of threads. The only requirement concerning the block of threads is that they must

[1] The thread is the basic element of processing

CUDA cores	128
CUDA Multiprocessors	8
Graphics Clock	738 MHz
Processor Clock	1836 MHz
Global Memory	512 MB
Memory Clock	1100 MHz
Memory Bandwidth	70.4 GB/s

Table 1. GTS 250 NVIDIA GPU main characteristics.

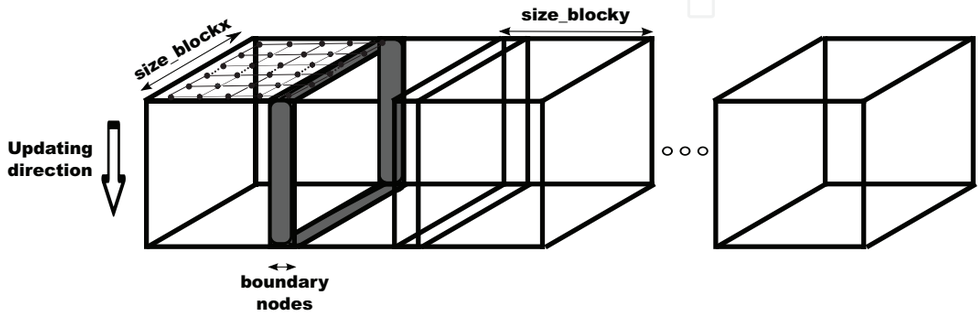

Fig. 7. Temperatures updating scheme on the GPU.

be independent from each other. Fig. 6 shows threads' hierarchy and its organization in the GPU.

3.2 GPU implementation of heat equation solver

GPU's structure fits perfectly our problem, where the full data can be split up in independent blocks that can be process the data in parallel. Each multiprocessor can work with a portion of grid's nodes increasing the performance of the system. The GPU used in this work was a GTS-250 from NVIDIA (cost around 250€- 300 $), whose characteristics are summarized in Table 1.

As was pointed, one of the main important aspects in an efficient CUDA-based system is the correct management of the memory to reduce the access to the global memory. To this aim the full grid of points, see Fig. 2(a), was divided into volume slices of size $size\_blockx \times size\_blocky$, where the nodes' temperature of each slice is computed in a block of threads, see Fig. 7. Each thread of the block is responsible for updating the temperature of the nodes with the same (x,y) coordinates within the considered piece of soil. The threads advance as a wavefront, updating the nodes' temperature starting from the superficial layers to the inside of the soil, see Fig 7. It can be noted that there are overlapping areas between different blocks of threads, labeled as *boundary nodes* and indicated in grey in Fig. 7, which must be taking into account to compute only once the new temperature value.

Concerning the memory usage, the initial temperatures are stored in the global memory, and they have been transferred from the HOST memory to GPU global memory prior to the computation of the new temperatures. The temperatures are duplicated in the memory, as during one iteration we need to use one location to read temperatures and the other to write

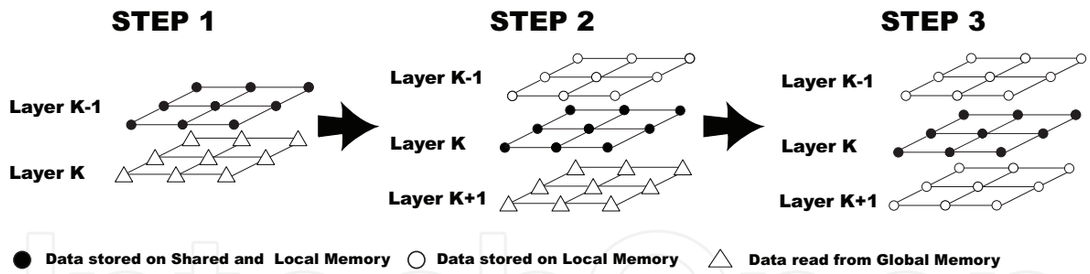

Fig. 8. Data memory transferences during the updating process.

the updated values and in the following iteration the roles are interchanged. The remainder constant values needed in the computations, such as F_0 and values related to the boundary conditions, see Eq. (14), are also stored in the global memory. The access to the global memory should be minimized to increase the speed of the computations, because the global memory has a high latency access. Thus, we use, during the updating process, the shared memory of the multiprocessors to accelerate the access to the data. The memory operations are shown in Fig. 8 where we can see the data transferences between the different memories of the GPU. In Fig. 8 we will consider the temperature updating process from nodes in *Layer K*. In *STEP 1* the temperatures of *Layer K-1* nodes are stored in both the multiprocessor's shared memory and in the cores' local memory. Moreover, nodes' temperatures from *Layer k* are read from the global memory and stored in the local cores' memory . During *STEP 2* the nodes' temperatures from *Layer K* replace those from *Layer K-1* in the shared memory, at the same time, the nodes' temperatures from *Layer K+1* are read from global memory and stored in cores' local memory. In *STEP 3* all data required to perform *Layer K* nodes' temperature updating is available on the local memory and shared memory. The same temperature of a *Layer K* is required to update the temperature of several nodes (the node itself and its north, south, west and east neighbors). If all nodes had to access global memory to read these values the process would be slowed, however once they are read from cores' local memory they are transferred to the shared memory, where they are available to all threads of the block, thus reducing the time access to the data. Once a thread has updated the temperature of a node, it uploads to the main memory the updated value and it continues computing the following temperature node updating. There is a synchronization process when a thread finishes one node's temperature updating because we must ensure that prior to continue with a node of the following layer all threads have finished the temperatures updating of the current layer.

4. Results

In this section we will introduce the results of the complete system. We divide this section into two main topics. On the one hand the results of the detection algorithm are shown for a scenario from the TNO Physics and Electronics Laboratory, Jong et al. (1999). On the other hand, we will show the performance of the GPU implementation and how it improves the usability of the detection system reducing the processing time.

4.1 Landmine detection algorithm

Next, we will show the result of the previously described detection algorithm to images acquired in a real test field. The scenario considered corresponds to the sand lane of the

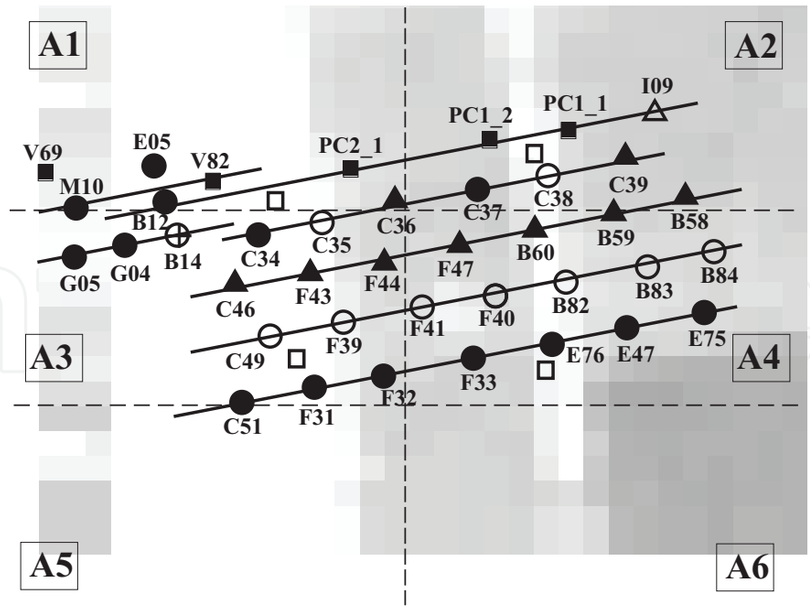

Fig. 9. Ground truth of the test field used during the experiment corresponding to a sand lane with different types of surrogated mines and non-mine targets.

Symbol	Category	Total
●	Surface mine	14
○	Mine at 1 cm	9
▲	Mine at 6 cm	9
⊕	Mine at 10cm	1
△	Mine at 15cm	1
■	Undefined test object	5
□	Shell marker	4

Table 2. Symbols used to represent the different categories of targets present in the test field in Fig. 9.

test facilities of the TNO Physics and Electronics Laboratory. For the experimental setup considered, the measured thermal diffusivity of the soil was $\alpha_{\text{sand}} = 6 \times 10^{-7}$ m^2/s. With respect to the test mine targets present, they are surrogated mines and most of them have been built at TNO-FEL. In all test mines the same substitute for the explosive has been used, RTV, having the same relevant properties as the real explosive and particularly $\alpha_{\text{RTV}} = 1.13 \times 10^{-7}$ m^2/s. Fig. 9 shows a sample image of the sand lane acquired with the IR sensor and the position of the different targets considered. Table 2 summarizes the symbols used for the different categories of targets present. The total number of targets is 43, 34 of which correspond to landmines. The remaining nine targets are five undefined test objects and four shells used as markers. We will concentrate on the results of the quasi-inverse and full-inverse procedures for the classification of mines and non-mine targets respectively.

Location	Detected and classified	Total
Surface	12	12
Buried at 1 cm	6	6
Buried at 6 cm	5	6
Buried at 10 cm	1	1
Buried at 15 cm	0	1

Table 3. Summary of the mines correctly detected and classified after the application of the quasi-inverse operator.

4.1.1 Results of the quasi-inverse operator for the classification of mine targets

The quasi-inverse operator classifies the detected targets as *Mine* or *Unknown*. Moreover, for the *Mine* class, sub-categories corresponding to their depth of burial are produced. For the experimental setup in Fig. 9, the results of the application of the quasi-inverse operator are summarized in Table 3, showing the distribution of mine targets correctly detected and classified according to their depth of burial with $e_{max} = 2.6$. As can be seen, all the mine targets on the surface or at 1cm depth were correctly detected and classified, and so were five out of six of the mines buried at 6 cm. The results for depths of 10 and 15 cm are not conclusive since only one of each is present, but a degraded performance of the quasi-inverse operator with depth is to be expected.

The performance of the classification operator is evaluated by making use of two properties, sensitivity and specificity, Hanley & McNeil (1982),

$$\text{Sensitivity} = \frac{TP}{TP + FN} \qquad \text{Specificity} = \frac{TN}{TN + FP} \tag{37}$$

being TP the number of true positives, TN the number of true negatives, FP the number of false positives and FN the number of false negatives. The performance depends strongly on the election of e_{max}, being a trade-off between sensitivity and specificity, i.e. , between the number of mine targets correctly classified and the number of false alarms. In humanitarian operations, the stress is put on the correct location of mines, while reducing the number of false alarms, although highly desirable, is a secondary goal. With respect to the global performance, it is clearly a function of the particular value of e_{max}. For $e_{max} = 2.6$ we find that 24 mines were correctly detected and classified over a total of 26.At the same time, the number of false positives is 13 compared to the 27 after the application of the detection stage alone.

4.1.2 Results of the full-inverse approach for the classification of non-mine targets

Now, we will illustrate the process of estimating the thermal parameters of non-mine targets making use of the full inverse process previously described. To this aim, we will consider the test object V82 present on the minefield (see Fig. 9). This target was classified as *unknown* by the quasi-inverse operator and we now aim to infer what type of object it is by estimating its thermal properties. If we estimate the measurement error to be $\delta = 0.3^{\circ}C$ and setting $\eta = 0.2$, we have,

$$\mu > 2\frac{1+\eta}{1-2\eta} = 4. \tag{38}$$

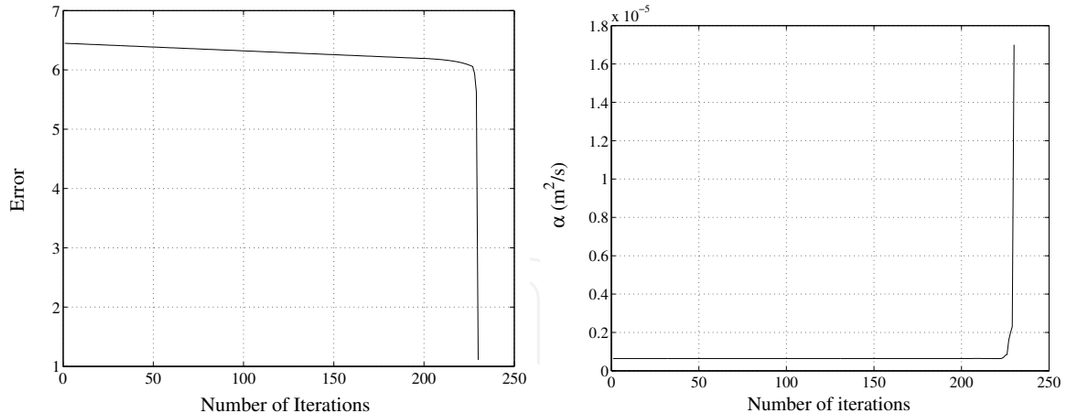

(a) (b)

Fig. 10. Test target V82: (a) Evolution of the error in the estimation of α; (b) Evolution of the value of α during the inverse problem procedure.

For $\mu = 4.1$, the discrepancy principle determines the stopping rule as,

$$\|y^\delta - F[p^\delta_{k(\delta,y^\delta)}]\| \leq 1.23 < \|y^\delta - F[p^\delta_k]\|, \quad 0 \leq k \leq k(\delta, y^\delta) \tag{39}$$

The evolution of the error for the Landweber iteration method is shown in figure 10(a). The stopping criteria in (39) corresponds to a number of iterations of the algorithm $N_{\text{it}} = 230$. Figure 10(b) shows the evolution of the estimation of the α parameter in this case. The final result obtained for the non-mine target V82 is,

$$\alpha_{\text{V82}} = 170 \times 10^{-7} \text{m}^2/\text{s}.$$

This value is two orders of magnitude bigger than that of the sand ($\alpha_{\text{sand}} \approx 6 \times 10^{-7} \text{m}^2/\text{s}$) which coincides with typical values of the thermal diffusivity of metallic solids.

4.2 GPU heat equation solver

We will now introduce the results obtained with the GPU implementation in terms of system throughput. As was pointed in the introduction a NVIDIA GTS 250 GPU, a low-cost GPU, was used to perform the comparison between a purely CPU implementation (Core2Duo 2.8 GHz implementation in C++) of the heat equation solver and a GPU implementation. One of the first issues is to think about the blocks threads' distribution and partitioning. The full volume of nodes which form the grid of points must be divided into blocks of threads, each of which is responsible for the nodes' temperature updating. The idea can be seen in Fig. 7, where the volume has been divided into blocks of threads of size *size_blockx*×*size_blocky* which are sent to the MP of th GPU, in this case a 1D array of blocks is shown for the shake of clarity. Fig. 11(a) shows the performance of the GPU for various block sizes, where we have chosen *size_blockx* = *size_blocky*, and a volume of 800×800×50 nodes. The results from these simulations can be seen in Table 4, where the speedup is compared to a purely CPU simulation of the full volume. It can be noted that the throughput of the system raises up as the size of the block is increased. This is due to the fact that when small blocks are used there are a lot

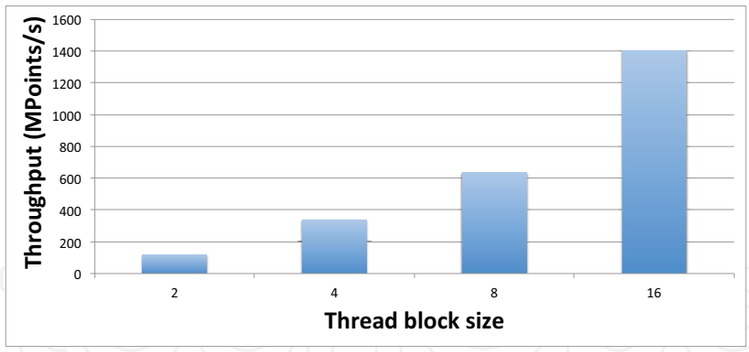

(a) Throughput of GPU heat equation solver for different blocks' size.

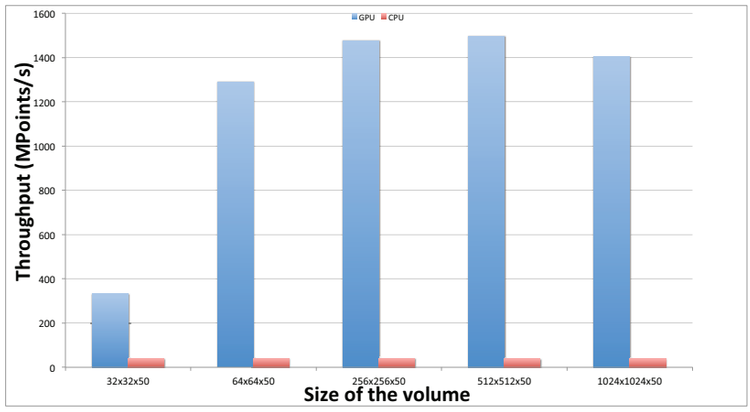

(b) Throughput of GPU and CPU heat equation solvers implementations for different volume of simulated points. In the GPU implementation the block grids' size was set to 16×16.

Fig. 11. Performance results comparing GPU and CPU throughputs for different setups.

of such small blocks spread over all MP, and therefore there will be a long cue of pending blocks to be processed. On the contrary, if the size of the blocks is increased we will have less blocks and the cue of pending blocks to be processed by the MP will be reduced. There is a limit, imposed by GPU's structure, given by the maximum number of threads that a MP can process (512). It can be seen from Fig. 11(a) and Table 4 that the throughput of the system is increased one order of magnitude when we go from 2×2 to 16×16 blocks of threads. Thus in the following simulations we will used this block's size for GPU simulations. Fig. 11(b) shows the GPU and CPU throughput for different nodes volumes, the data can be seen in Table 5. It can be noted how the performance of the GPU grows up one order of magnitude when the size of the volume is increased. This is due to the fact that for small volume of nodes not all GPU's resources are being used, whereas for big enough size volumes the inherent parallelism of the GPU increases the throughput of the system. It is obvious that for very big volumes the throughput will be low because there will be a cue of pending blocks to be processed which degrades the throughput of the system (note the reduction of the throughput for the 1024×1024×50 volume).

block_dimx × block_dimy	GPU throughput (Mpoints/s)	GPU time (s)	Speedup
2×2	120.0	25.6	3.1
4×4	336.5	9.1	8.7
8×8	634.3	4.8	16.7
16×16	1400.0	2	40

Table 4. GPU throughput for a given volume of points and varying block thread's dimensions.

Volume	GPU throughput (Mpoints/s)	CPU throughput (Mpoint/s)	Speedup
32×32×50	332	39.3	8.4
64×64×50	1289.33	39.3	32.6
256×256×50	1476.67	39.3	37.0
512×512×50	1496.02	39.3	39.3
1024×1024×50	1402.8	39.3	36.7

Table 5. Throughput and CPU and GPU solvers of the heat equation solver for different size volumes.

5. Conclusions

In this chapter, two inverse procedures for the inspection of soils by non-invasive means with application in antipersonnel mines detection have been presented. The first quasi-inverse procedure aims at the detection of surface-laid and shallowly buried mines, giving an estimation of their depth of burial that will be of critical importance during the removal stage. In the second approach, a full inverse procedure for the identification of the thermal properties of other objects present on the soil was presented. Both procedures need the recursive solution of the heat equation problem for different soil configurations, which constitutes a very time consuming task on a conventional computer. The efficient solution of the aforementioned procedures is successfully solved using a heat equation solver accelerator based on the use of GPUs, obtaining speed-up factors over 40. The speedup obtained with the proposed system with respect to nowadays computers, together with its low-cost and portability justifies the implementation as it permits its use on the field during demining operations.

6. References

Bach, P., Toumeur, P. L., Poumarkde, B. & Bretteand, M. (1996). Neutron activation and analysis, *EUREL International Conference Detection of Abandoned Landmines*, Vol. 431, pp. 58–61.

Bejan, A. (1993). *Heat Transfer*, John Wiley & Sons, Inc.

Cameron, M. & Lawson, R. (1998). *To Walk Without Fear: The Global Movement to Ban Landmines*, Toronto: Oxford University Press.

Durbano, J., Ortiz, F., Humphrey, J. R., Curt, P. & Prather, D. (2004). Fpga-based acceleration of the 3d finite-difference time-domain method, *Proceedings of the 12th annual IEEE symposium on Field-Programmable Custom Computing Machines*, pp. 156–163.

Engl, H. W., Hanke, M. & Neubauer, A. (1996). *Regularization of Inverse problems*, Kluwer Academic Publishers.

England, A., Galantowiz, J. & Schretter, M. (1992). The radiobrightness thermal inertia measure of soil moisture, *IEEE Transactions on Geoscience and Remote Sensing* 30(1): 132–139.

England, A. W. (1990). Radiobrigthness of diurnally heated, freezing soil, *IEEE Transactions on Geoscience and Remote Sensing* 28(4): 464–476.

Englelbeen, A. (1998). Nuclear quadrupole resonance mine detection, *CLAWAR'98*, pp. 249–253.

Furuta, K. & Ishikawa, J. (eds) (2009). *Anti-personnel landmine detection for humanitarian demining: the current situation and future direction for Japanese research and development*, Springer-Verlag.

Gros, B. & Bruschini, C. (1998). A survey on sensor technology for landmine detection, *Journal of Humanitarian Demining* pp. 172–187.

Hanley, J. & McNeil, B. (1982). The meaning and use of the area under a receiver operating characteristic (ROC) curve, *Radiology* 143: 29–36.

Horowitz, P. (1996). New technological approaches to humanitarian demining, *Technical Report JSR-96-115*, JASON MITRE.

Hwu, W. W., Keutzer, K. & Mattson, T. (2008). The concurrency challenge, *IEEE Design & Test of Computers* 25(4): 312 – 320.

ICBL (2006). *Landmine Monitor Report 2006*, International campaign to can landmines (ICBL).

Incropera, F. & DeWitt, D. (2004). *Introduction to Heat Transfer*, 4th edn, John Wiley & Sons.

Jankowski, P., Mercado, A. & Hallowell, S. (1992). FAA explosive vapor/particle detection technology, *Applications of Signal and Image Processing in Explosives Detection Systems*, Vol. 1824, pp. 13–27.

Jong, W., Lensen, H. & Janssen, H. (1999). Sophisticated test facilities to detect land mines, *Detection and Remediation Technologies for Mines and Minelike Targets IV*, Vol. 3710 of *Proceedings of the SPIE*, pp. 1409–1418.

Kahle, A. B. (1977). A simple thermal model of the earth's surface for geologic mapping by remote sensing, *Journal of Geophysical Research* 82: 1673–1680.

Khanafer, K. & Vafai, K. (2002). Thermal analysis of buried land mines over a diurnal cycle, *IEEE Transactions on Geoscience and Remote Sensing* 40(2): 461–473.

Kirsch, A. (1996). *An introduction to the Mathematical Theory of Inverse problems*, Vol. 120 of *Applied mathematical sciences*, Springer-Verlag, New York.

Larsson, C. & Abrahamsson, S. (1993). Radar, multispectral and biosensor techniques for mine detection, *Symposium on Anti-Personnel Mines*, pp. 179–202.

Liou, Y. & England, A. (1998). A land surface process/radiobrightness model with couple heat and moisture transport for freezing soils, *IEEE Transactions on Geoscience and Remote Sensing* 36(2): 669–677.

Lockwood, G., Shope, S., Bishop, L., Selph, M. & Jojola, J. (1997). Mine detection using backscatered x-ray imaging of antitank and antipersonnel mines, *Detection and Remediation Technologies for Mines and Minelike Targets II* 3079: 408–417.

López, P. (2003). *Detection of Landmines from Measured Infrared Images using Thermal Modeling of the Soil*, PhD thesis, Universidad de Santiago de Compostela.

López, P., Pardo, F., Sahli, H. & Cabello, D. (2009). Non-destructive soil inspection using an efficient 3d softwareâĂŞhardware heat equation solver, *Inverse Problems in Science and Engineering* 6(17): 755–775.

López, P., van Kempen, L., Sahli, H. & Cabello, D. (2004). Improved thermal analysis of buried landmines, *IEEE Transactions Geoscience and Remote Sensing* 42(9): 1955–1964.

Maksymonko, G. B. & Le, N. (1999). Performance comparison of standoff minefield detection algorithms using thermal IR image data, Vol. 3710, SPIE, pp. 852–863.
URL: *http://link.aip.org/link/?PSI/3710/852/1*

NVIDIA (2010). *NVIDIA CUDA C Programming Guide 3.1*, NVIDIA Corporation Technical Staff.

Ottawa (1997). Convention on the prohibition of the use, stockpiling, production and transfer of anti-personnel mines and on their destruction.

Pardo, F., López, P., Cabello, D. & Balsi, M. (2009). Effcient software-hardware 3d heat equation solver with applications on the non-destructive evaluation of minefields, *Computers & Geoscience* 35: 2239–2249.

Pardo, F., López, P., Cabello, D. & Balsi, M. (2010). Fpga computation of the 3d heat equation, *Computational Geoscience* 14: 649–664.

Placidi, P., Verducci, L., Matrella, G., Roselli, L. & Ciampiolini, P. (2002). A custom VLSI architecture for the solution of FDTD equations, *IEICE Transactions on Electronics* E85-C: 572–577.

Pregowski, P., Walczack, W. & Lamorski, K. (2000). Buried mine and soil temperature prediction by numerical model, *Proceedings of the SPIE, Detection and Remediation Technologies for Mines and Minelike Targets V*, Vol. 4038, pp. 1392–1403.

Robledoa, L., Carrascoa, M. & Merya, D. (2009). A survey of land mine detection technology, *International Journal of Remote Sensing* 30(9): 2399–2410.

Sabatier, J. & Xiang, N. (2001). An investigation of a system that uses acoustic seismic coupling to detect buried anti-tank mines, *IEEE Transactions on Geoscience and Remote Sensing* 39(6): 1146–1154.

Schneider, R., Turner, L. & Okoniewski, M. (2002). Application of FPGA technology to accelerate the Finite-Difference Time-Domain (FD-TD) method, *Proceedings of the 10th ACM/SIGDA International Symposium on Field-Programmable Gate Arrays*, pp. 97–105.

Siegel, R. (2002). Land mine detection, *IEEE Instrumentation & Measurement Magazine* pp. 22–28.

Thanh, N., Hao, D. N. & Sahli, H. (2009). *Augmented Vision Perception in Infrared Algorithms and Applied Systems*, Advances in Pattern Recognitiob, SpringerLink, chapter Infrared Thermography for Land Mine Detection, p. 471.

Thanh, N., Sahli, H. & Hao, D. (2007). Finite-Difference methods and validity of a thermal model for landmine detection with soil propierty estimation, *IEEE Transactions on Geoscience and Remote Sensing* (4): 656–674.

Thanh, N., Sahli, H. & Hao, D. (2008). Infrared thermography for buried landmine detection: inverse problem settin, *IEEE Transactions on Geoscience and Remote Sensing* (12): 3987–4004.

Vines, A. & Thompson, H. (1999). Thompson, beyond the landmine ban: Eradicating a lethal legacy, *Technical report*, Research Institute for the Study of Conflict and Terrorism.

Wang, T. & Chen, C. (2002). 3-D thermal-ADI: A linear-time chip level transient thermal simulator, *IEEE Transactions on Computer-Aided Design of Integrated Circuits and Systems* 21(12): 1434–1445.

Zoubir, A. M. & Iskander, R. (2004). *Bootstrap Techniques for Signal Processing*, Cambridge University Press.

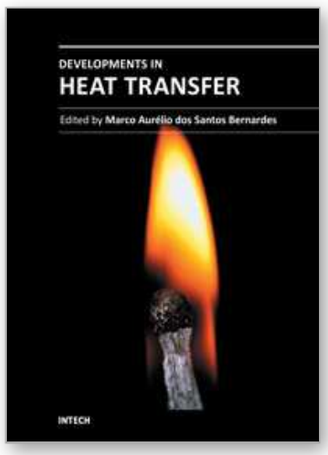

Developments in Heat Transfer

Edited by Dr. Marco Aurelio Dos Santos Bernardes

ISBN 978-953-307-569-3
Hard cover, 688 pages
Publisher InTech
Published online 15, September, 2011
Published in print edition September, 2011

This book comprises heat transfer fundamental concepts and modes (specifically conduction, convection and radiation), bioheat, entransy theory development, micro heat transfer, high temperature applications, turbulent shear flows, mass transfer, heat pipes, design optimization, medical therapies, fiber-optics, heat transfer in surfactant solutions, landmine detection, heat exchangers, radiant floor, packed bed thermal storage systems, inverse space marching method, heat transfer in short slot ducts, freezing an drying mechanisms, variable property effects in heat transfer, heat transfer in electronics and process industries, fission-track thermochronology, combustion, heat transfer in liquid metal flows, human comfort in underground mining, heat transfer on electrical discharge machining and mixing convection. The experimental and theoretical investigations, assessment and enhancement techniques illustrated here aspire to be useful for many researchers, scientists, engineers and graduate students.

INTECH
open science | open minds

InTech Europe
University Campus STeP Ri
Slavka Krautzeka 83/A
51000 Rijeka, Croatia
Phone: +385 (51) 770 447
Fax: +385 (51) 686 166
www.intechopen.com

InTech China
Unit 405, Office Block, Hotel Equatorial Shanghai
No.65, Yan An Road (West), Shanghai, 200040, China
中国上海市延安西路65号上海国际贵都大饭店办公楼405单元
Phone: +86-21-62489820
Fax: +86-21-62489821

IntechOpen